Journal of Materials Chemistry A

ROYAL SOCIETY OF CHEMISTRY

PAPER

View Article Online
View Journal

Check for updates

Cite this: DOI: 10.1039/d5ta06515a

Binder-free nickel–iron selenide catalyst arrays for coupling hydrogen production with polyethylene terephthalate plastic electro-upcycling

Pooja J. Sharma,[a] Sanjay A. Bhakhar,[a] Meghana N. Patel,[b] Manish N. Nandpal,[b] Kaushik A. Bhakhar,[c] Samir G. Patel,[b] Parikshit Sahatiya,[d] Goli Nagaraju,[e] C. K. Sumesh[a] and Pratik M. Pataniya *[a]

The rational design and optimization of electrode structures are crucial for enhancing catalytic performance for water electrolysis and plastic upcycling, addressing environmental concerns while creating economic value. In this work, a hierarchically structured Ni–Fe_3Se_4 catalyst was deposited on nickel foam by a chemical bath deposition method. The Ni–Fe_3Se_4 catalyst exhibits low interfacial resistance and abundance of NiFeOOH active sites, achieving excellent electrocatalytic performance for industrial-level alkaline water electrolysis and electrocatalytic polyethylene terephthalate (PET) upcycling with conversion of ethylene glycol to formate with a faradaic efficiency of 89%. A bi-functional electrolyser using Ni–Fe_3Se_4 demonstrates excellent stability at 300 mA cm^{-2} over 42 hours in a 5 M KOH electrolyte. Interestingly, the Ni–Fe_3Se_4 catalyst shows the simultaneous anodic electro-upcycling of PET hydrolysate and cathodic H_2 production at industrial scale current densities for 50 hours, ensuring sustained performance for transforming waste into value-added products such as H_2-gas, formate, and terephthalate.

Received 12th August 2025
Accepted 15th November 2025

DOI: 10.1039/d5ta06515a

rsc.li/materials-a

Open Access Article. Published on 19 November 2025. Downloaded on 12/13/2025 9:16:47 AM.
This article is licensed under a Creative Commons Attribution 3.0 Unported Licence.

Introduction

The widespread use of plastics, particularly polyethylene terephthalate (PET), has created considerable environmental challenges. PET is widely used in packaging, textiles, and other consumer items due to its durability, lightweight nature, and exceptional barrier properties.[1–3] However, its extensive utilization has led to substantial waste accumulation, greatly contributing to environmental pollution and posing a threat to ecosystems and human health.[4,5] Furthermore, microplastics are seriously harming ecosystems and posing severe implications for human health.[6] Consequently, developing efficient and sustainable strategies for managing PET waste has become imperative.[1] Conventionally, recycling of PET plastics has been processed by mechanical and chemical processes. However, the challenges such as low quality of recycled PET, demands of high energy and utilization of hazardous chemicals are raising concerns with their environmental and economic viability. Encouragingly, the electrocatalytic upgrading has emerged as a promising approach for PET recycling, offering high control, functioning under mild operation conditions at ambient temperature and pressure, low-cost energy input, and product selectivity.[7] The electrocatalytic upgrading of PET involves two steps: first, its de-polymerization into terephthalate (TPA) and ethylene glycol (EG) in the alkaline solution[8,9] and subsequently, the electrochemical oxidation of EG into formate at the anode and coupling the hydrogen evolution reaction (HER)[10–12] or reduction of CO_2 (CO_2RR) at the cathode.[13,14]

The strategy of producing the cathodic green hydrogen fuel coupled with anodic plastic electro-upcycling during the electrolysis offers an efficient solution for the universal problem of pollution and energy crisis.[10–12] Apart from this, the selective PET derived EG assisted water electrolysis led to the energy-saving approach for H_2-generation. The ethylene glycol oxidation reaction (EGOR) exhibits a low oxidation potential of 0.57 V *vs.* RHE (reversible hydrogen electrode),[15] which is significantly smaller as compared to that for the oxygen evolution reaction (1.23 V *vs.* RHE), saving the energy for electrolysis.[11] However, the efficiency and selectivity of the HER and EGOR rely on the performance of the electrocatalysts. The sustainable electrocatalytic process demands stable catalysts with an abundance of catalytically active surface area for better adsorption capabilities for both EG and reactive oxygen species (OH_{ads}), high

[a]Department of Physical Sciences, PD Patel Institute of Applied Sciences, Charotar University of Science and Technology, CHARUSAT, Changa, Gujarat, India. E-mail: pm.pataniya9991@gmail.com

[b]Department of Pharmaceutical Chemistry and Analysis, Ramanbhai Patel College of Pharmacy, Charotar University of Science and Technology, CHARUSAT, Changa, Gujarat, India

[c]Gandhinagar Institute of Pharmacy, Gandhinagar University, Gandhinagar, Gujarat 382721, India

[d]Department of Electrical and Electronic Engineering, BITS Pilani Hyderabad, Secunderabad 500078, India

[e]Department of Materials, Imperial College London, London, SW72AZ, UK

Open Access Article. Published on 19 November 2025. Downloaded on 12/13/2025 9:16:47 AM.
This article is licensed under a Creative Commons Attribution 3.0 Unported Licence.

conductivity to ensure the efficient charge transfer on the electrode and exceptional intrinsic performance with accelerated kinetics.[16–19] The noble metal (*e.g.* Pt and Pd) based materials have shown the EGOR performance and PET plastic electro-upcycling. However, problem with EG oxidation on Pt and Pd is the catalyst poisoning due to accumulation of poisonous carbonyl species.[20,21] Encouragingly, catalytic networks comprising transition metals such as Ni, Co and Cu have been explored previously to prevent the catalyst poisoning by cleaving the C–C bond in EG and producing the value added product such as formate.[22] Additionally, the abundance of transition metals on the earth encourages researchers to extend the electrocatalytic applications to the industrial scale at significantly low production cost.[23]

Generally, the transition metal-based catalysts exhibit inferior catalytic performance than the Pt-based catalysts. Currently, porous catalytic networks based on multi-metals in conjunction with non-metal elements are promising for enhanced performance due to multi-active sites, synergistic improvements in the charge transfer, and enhanced corrosion resistance.[24] *E.g.* Wenbo Li *et al.* reported a strategy for designing the hierarchical heterostructure Ni-MOF@MnCo–OH for highly selective EG oxidation and upgrading the PET at industrial scale current density.[11] The vertically oriented $NiCo_2O_4$ nanosheets synthesized by a hydrothermal technique demonstrated greatly selective oxidation of PET-hydrolysate and production of formate with a faradaic efficiency of more than 90%.[13] Promisingly, NiOOH, CuOOH and CoOOH species formed *in situ* on the surface of catalysts, produced due to oxidation of metal M^{2+} to M^{3+} effectively serve as active sites for the advanced oxidation reaction.[25–28] Hongxing Kang *et al.* reported the fabrication of NiCu@NF utilizing electrochemical deposition of Cu-species on Ni foam and *in situ* formation of NiOOH and $CuOOH/Cu(OH)_2$ (ref. 9) species during EG oxidation. Although, metal hydroxide/oxyhydroxide species are active sites for advanced oxidation,[25,26] they are suffered from the higher charge-transfer resistance as well as inferior HER performance.[29] Therefore, to design the optimized catalysts that are active for both the HER and EGOR is an open challenge.

Among transition metal-based electrocatalysts, transition metal selenide (TMSe) emerged as a highly efficient candidate for water-splitting applications. This can be attributed to the unique electronic configuration of selenium ($4s^2p^4$), whose unoccupied 3d orbitals enable covalent bonding interactions with transition metal atoms, thereby facilitating rapid electron transport and accelerating electrochemical reactions during water electrolysis.[30,31] Moreover, the relatively low electronegativity of selenium enhances OH^- diffusion at the catalytic sites, simultaneously improving the intrinsic metallicity of selenides and boosting charge-transfer kinetics. In addition, the comparatively larger ionic radius of selenium contributes to further enhancement of the electrocatalytic activity of TMSe systems.[32,33] For instance, Wang *et al.* employed a facile selenization strategy to integrate bimetallic $CoSe_2$–$FeSe_2$ nanoparticles with heterogeneous architectures onto carbon nanotubes, effectively lowering the energy barrier of the OER process.[34] Similarly, Mohanty *et al.* synthesized selenium-rich $Ni_{0.7}Fe_{0.3}Se_2$ *via* Fe incorporation into $NiSe_2$ using a hydrothermal route, demonstrating that both Fe doping and selenium vacancies significantly improved electrical conductivity, reduced the free energy of reaction intermediates, increased the density of states near the Fermi level, and ultimately enhanced OER performance.[35]

Inspired from this, we explored the electro-upcycling of PET plastic and H_2-production using nickel–iron selenide (Ni–Fe_3Se_4) catalysts. This catalyst possesses desirable properties for catalyzing the HER, OER, EGOR, and, PETOR, exhibiting low interfacial resistance and an abundance of catalytically active sites. The Ni–Fe_3Se_4 catalyst demonstrates a remarkably low overpotential of 174 mV for the HER and 164 mV for the OER at 10 mA cm^{-2}, indicative of its superior catalytic activity compared to previously reported catalysts. Owing to corrosion resistive ability and dimensional stability, Ni–Fe_3Se_4 demonstrates water electrolysis under industrial-level alkaline conditions (5 M KOH) and at industrial-scale current density. The electrode stability was measured at 300 mA cm^{-2} for a time interval of more than 42 hours. Additionally, EG electrolysis at 1.667 V in 1 M KOH + 0.3 M EG enabled PET plastic electro-upcycling at a current density of 100 mA cm^{-2}, yielding value-added products such as formate and terephthalate. The faradaic efficiency for conversion of EG to formate is found to be 89% and 84% at current densities of 50 and 100 mA cm^{-2}, respectively.

Experimental

Materials and methods for synthesis of Ni–Fe_3Se_4

For the synthesis of Ni–Fe_3Se_4 catalysts, 1.5 mM $FeSO_4 \cdot 6H_2O$ (0.417 g) and 2.0 mM Na_2SeO_3 (0.346 g) were dissolved in 50 mL distilled water. After this, 1 mL ammonia solution was added to the precursor solution and the solution was stirred for 20 minutes at room temperature. Meanwhile, nickel foam (NF) of dimension 3.5 × 2.5 cm^2 was cleaned using 2.5 M HCl solution, distilled water, and ethanol to remove the impurities and oxide layer from NF. The precursor solution and pre-treated NF were then transferred to a 100 mL Pyrex glass bottle and heated at 85 °C using a preheated hot-air oven for 15 hours. The Ni–Fe_3Se_4 electrodes were then cleaned using distilled water and ethanol. Finally, the electrodes were sonicated for 5 minutes to remove loosely attached catalyst particles and dried at 70 °C in a vacuum oven (10^{-2} to 10^{-3} torr). Control electrodes without an iron source were fabricated using a similar technique and labelled as NiSe, while the electrode fabricated without a Se source is labelled as Ni–Fe_3O_4.

Materials characterization

The structure of the Ni–Fe_3Se_4 catalyst was studied by powder XRD using a D2-phaser with Cu Kα radiation. The morphology and chemical purity of the as-synthesized catalysts were investigated using a scanning electron microscope (Make: FEI, LoVac Apreo electron microscope) with SEM-EDS facility. Elemental mapping of elements including Fe, Ni, Se, and O was also recorded. The surface chemical composition was further

 This journal is © The Royal Society of Chemistry 2025

Open Access Article. Published on 19 November 2025. Downloaded on 12/13/2025 9:16:47 AM.
This article is licensed under a Creative Commons Attribution 3.0 Unported Licence.

investigated on a Thermo Scientific K-alpha XPS (X-ray photoelectron spectrometer).

Preparation of PET hydrolysate

To prepare the PET hydrolysate, outdated plastic has to be treated. First, a 4 g water bottle was washed with detergent to remove dust, labels, and other contaminants. It was then cut into small pieces (1×1 cm^2) and added to 50 mL of 2 M KOH solution, followed by continuous stirring for 30 minutes at room temperature. The mixture was then transferred to a Teflon container and heated at 160 °C for 15 hours. Afterward, an additional 50 mL of water was added to dilute the PET hydrolysate. The final solution was then filtered and used for electrochemical upcycling.

Electrochemical measurements

The electrochemical performance of Ni–Fe_3Se_4, NiSe, Ni–Fe_3O_4, commercial Pt/C and commercial RuO_2 catalysts for water electrolysis and PET plastic up-cycling was measured using a Metrohm PGSTAT-M204 electrochemical workstation. First, kinetics of water and EG electrolysis was studied in 1 M KOH and 1 M KOH + 0.3 M EG, respectively, using the standard three electrode system with Ni–Fe_3Se_4 electrodes, Ag/AgCl (3 M KCl saturated) and Pt/C as working, reference and counter electrodes, respectively. The linear sweep voltammetry (LSV) curves were recorded at scan rate of 2 mV s^{-1}. The polarization curves with *iR*-compensation were calculated. The Tafel slope was also calculated from polarization curves for the study of kinetics of the HER, OER, EGOR and PETOR. The calculation of interfacial resistance and study of charge transport were accomplished using electrochemical impedance spectroscopy in the frequency range of 100 kHz to 10 mHz with an amplitude of 10 mV. Cyclic-voltammetry curves were recorded in the non-faradaic potential range at different scan rates ranging from 20 to 100 mV s^{-1}. The electrochemical surface area (ECSA) was also calculated using the C_{dl} value obtained from the CV curves. The stability of the electrode, efficiency of charge and mass transport was also studied using the multi-step chronopotentiometry at different current densities ranging from 10 to 100 mA cm^{-2}. *In situ* Raman spectroscopy using an i-Raman Plus (Make: BWTEK) and VIONIC (Make: Metrohm) system in the potential range of 1.3 to 1.6 V *vs.* RHE in 1 M KOH with and without 0.3 M EG. A two-electrode alkaline electrolyser with Ni–Fe_3Se_4 as both the anode and cathode was prepared for the study of overall water, EG and PET electrolysis. The water electrolysis was studied by LSV, EIS, and multi-step chronopotentiometry in different alkaline electrolytes (1 M, 3 M and 5 M KOH) at different temperatures from ambient temperature (25 °C) to 60 °C. The industrial-scale water electrolysis was studied by a stability test at a current density of 300 mA cm^{-2} for the time interval of more than 42 hours.

Analysis of products of ethylene glycol and PET hydrolysate electrolysis

The 1 M KOH + 0.3 M EG electrolyte was analysed by Raman spectroscopy using 532 nm excitation before and after electrolysis. The PET hydrolysate and TPA collected from PET hydrolysate were also tested by Raman spectroscopy. EG electrolyte was further investigated using a Waters Alliance High-Performance Liquid Chromatographic System (Australia) equipped with a PDA detector fitted with a quaternary gradient pump, degasser, column oven, autosampler and Shodex SH-1011 Sugar Column. Details of the HPLC measurements are given in the SI. Furthermore, ^{1}H NMR spectra were measured for the qualitative analysis of EG and PET electrolytes.

Results and discussion

The nickel–iron selenide (Ni–Fe_3Se_4) catalyst on the 3D-scaffold of the Ni foam was synthesized using chemical bath deposition (CBD). The schematic of synthesis process and digital image of the prepared catalysts are presented in Fig. 1a and S1, SI, respectively. Due to high electric conductivity, open porosity and ability to load higher amounts of catalysts, Ni foam was selected for the current collector for the electrolysis. Ni–Fe_3Se_4 catalysts were directly synthesized on Ni foam using $FeSO_4 \cdot 6H_2O$, and Na_2SeO_3 as Fe and Se sources in the presence of ammonia solution to provide alkaline conditions at a temperature of 85 °C for 15 h to optimize the mass loading of the catalysts. The chemical reaction for synthesizing Ni–Fe_3Se_4 is as follows:

$$3FeSO_4 + 6Na_2SeO_3 + 3NH_4OH \rightarrow Fe_3Se_4 + 2SeO_2 + 3Na_2SO_4 + 6NaO_2 + 3NH_3\uparrow + 3H_2O + O_2\uparrow \quad (1)$$

Simultaneously, the Fe^{3+} ions formed in alkaline precursor solution corrode the Ni foam because the reduction potential of the Fe^{3+} ions ($Fe^{3+} + e^- \rightarrow Fe^{2+}$; +0.77 V) is higher than that of nickel ($Ni^{2+} + 2e^- \rightarrow Ni$; −0.26 V). Apart from this, Ni foam also reacts with oxygen present in the solution and forms OH^-, leading to the incorporation of Ni^{2+} into the grown catalyst.[36] Therefore, the catalyst is labelled as Ni–Fe_3Se_4. The morphology of the catalyst was first observed by SEM (Fig. 1b–d). The rough surface of the NF suggests that the surface of the current collector is fully covered by the catalyst, which is beneficial for the efficient charge and mass transport during the electrolysis. As shown in Fig. 1c, the deposited Ni–Fe_3Se_4 system shows agglomerated nanostructures with granular features, suggesting the formation of interconnected clusters that enhance electron transport pathways. Moreover, the deposited Ni–Fe_3Se_4 showed faceted nanocrystals with sharp edges and uniform deposition on Ni foam, and such hierarchical structures could be expected to ensures abundant catalytically active sites, improved charge transfer, and enhanced stability. The morphologies of the NiSe and Ni–Fe_3O_4 catalysts are shown in Fig. S2 (SI). The chemical composition and electronic states of the constituent were further analysed by XPS. Fig. 1e presents the XPS survey of Fe 2p, showing the presence of peaks at 711.07 eV and 724.44 eV, which are ascribed to $2p_{3/2}$ and $2p_{1/2}$ orbits of Fe^{2+}. Furthermore, peaks centred at binding energies of 713.21 eV and 726.45 eV are related to the presence of Fe^{3+} $2p_{3/2}$ and Fe^{3+} $2p_{1/2}$ orbitals, respectively, showing the presence

Open Access Article. Published on 19 November 2025. Downloaded on 12/13/2025 9:16:47 AM.
This article is licensed under a Creative Commons Attribution 3.0 Unported Licence.

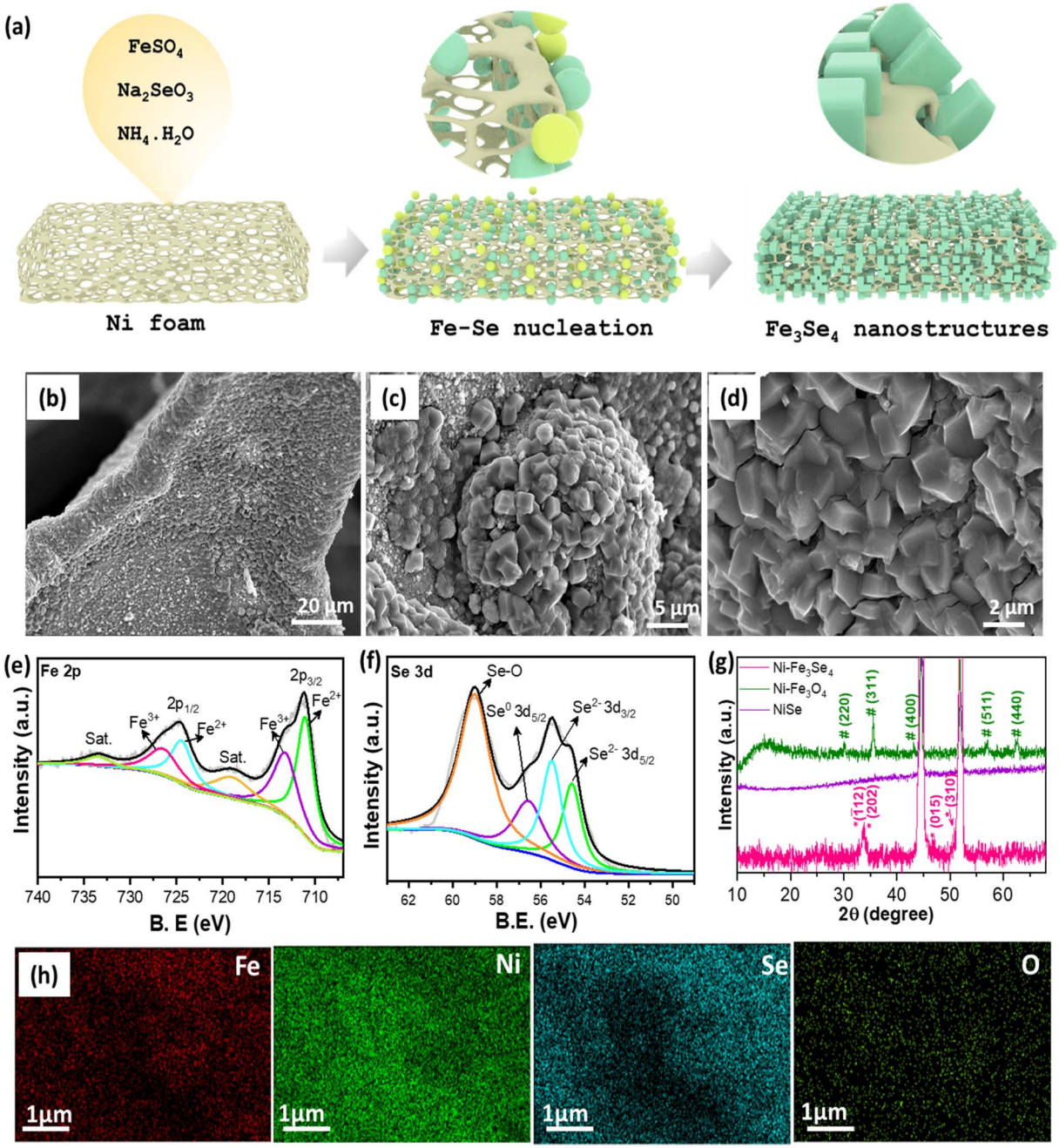

Fig. 1 (a) Schematic of the synthesis of the Ni–Fe_3Se_4 catalyst on the Ni scaffold, (b–d) SEM images of the Ni–Fe_3Se_4 catalyst, XPS survey of the Ni–Fe_3Se_4 catalyst: (e) Fe 2p and (f) Se 3d, (g) powder XRD patterns of Ni–Fe_3Se_4 and control electrodes, and (h) SEM-EDS mapping of Fe, Ni, Se and O elements of the Ni–Fe_3Se_4 catalyst.

of the Fe^{3+} electronic state. Additionally, the shakeup satellite peaks of Fe are observed at binding energies of 718.96 eV and 733.44 eV. Fig. 1f shows the deconvolution of Se 3d, containing the peaks at binding energies of 54.58 eV and 55.48 eV, related to Se^{2-} $3d_{5/2}$ and Se^{2-} $3d_{3/2}$ orbitals. Additionally, a peak at 56.58 eV shows the co-presence of Se^0 in the catalyst. The shakeup satellite is observed at a binding energy of 58.98 eV. The XPS O 1s survey is shown in Fig. S3b (SI). The XPS survey of Ni 2p shows a peak at 853.18 eV due to the presence of metallic Ni^0 phase (Fig. S3a, SI). The peaks centred at 856.08 eV and 873.88 eV are assigned to Ni $2p_{3/2}$ and Ni $2p_{1/2}$ of the Ni^{2+}-electronic state. Additionally, peaks at 856.08 eV and 879.68 eV are satellite peaks. In addition, the XPS spectra of the NiSe and Ni–Fe_3O_4 electrodes are displayed in Fig. S5 (SI). Furthermore, the structure of the Ni–Fe_3Se_4 catalysts and control catalysts was investigated by the powder XRD pattern (Fig. 1g). The XRD pattern of Ni–Fe_3Se_4 is indexed to the monoclinic structure. The XRD pattern is well matched with previous reports and aligns with the standard data (ICSD no. 96-153-7571).[37] Additional peaks at 44.6° and 52.0° are due to underlying Ni foam.[38] The

Open Access Article. Published on 19 November 2025. Downloaded on 12/13/2025 9:16:47 AM.
This article is licensed under a Creative Commons Attribution 3.0 Unported Licence.

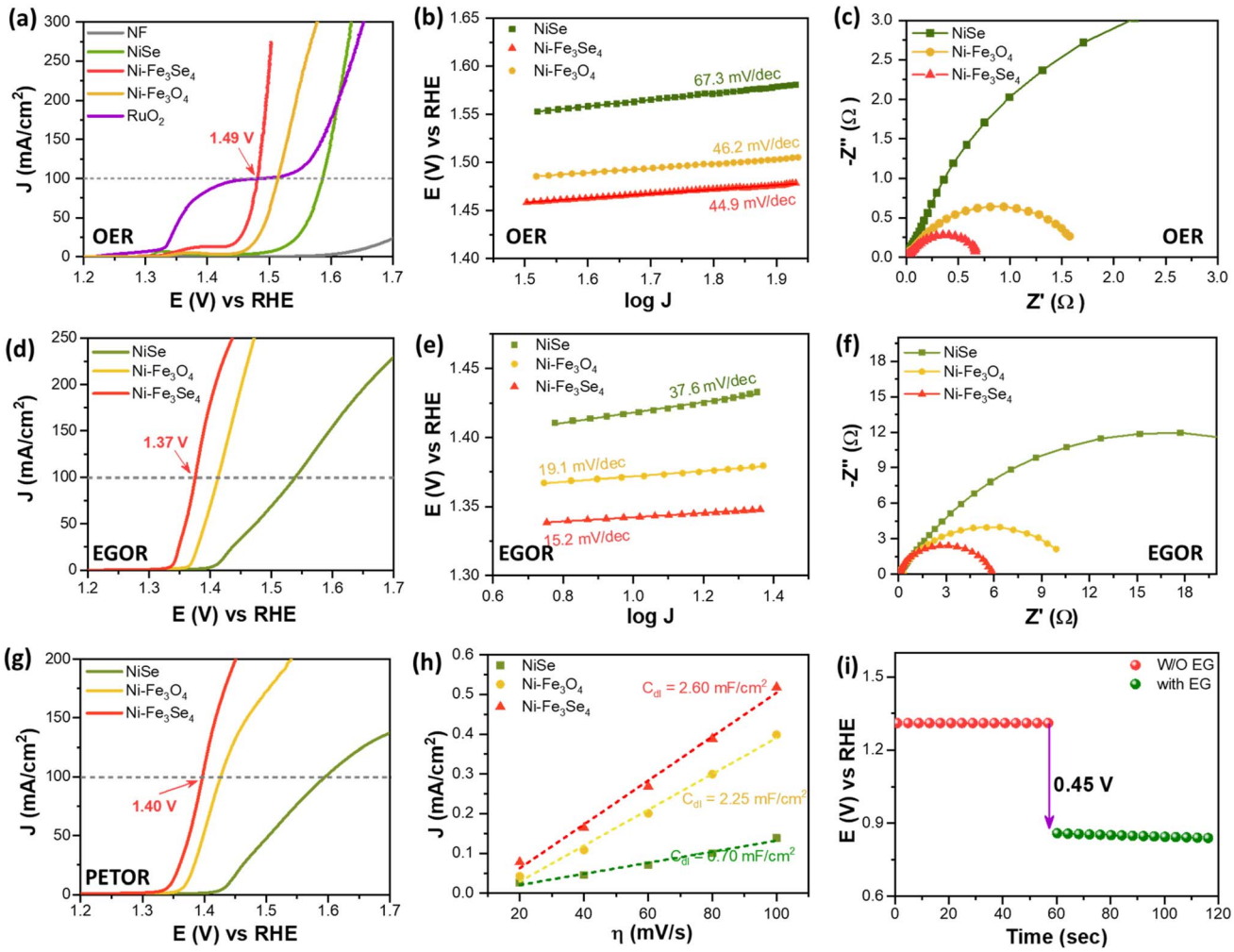

Fig. 2 (a) Polarization curves for OER activity on Ni–Fe_3Se_4, NiSe, Ni–Fe_3O_4, bare NF and commercial RuO_2 electrodes, (b) Tafel plots for OER performance of all the electrodes, (c) EIS spectra measured at 1.5 V *vs.* RHE in 1 M KOH, (d) polarization curves for EGOR activity on Ni–Fe_3Se_4, NiSe, and Ni–Fe_3O_4, (e) Tafel plots for EGOR performance, (f) EIS spectra measured at 1.35 V *vs.* RHE in 1 M KOH with 0.3 M EG, and (g) polarization curves for PETOR activity on Ni–Fe_3Se_4, NiSe, and Ni–Fe_3O_4, (h) ΔJ *vs.* scan rate for evaluation of double layer capacitance (C_{dl}), and (i) open circuit potential in 1 M KOH with and without (W/O) EG.

control electrode fabricated without a Se source exhibits a cubic inverse spinel structure of magnetite (Ni–Fe_3O_4)[39] and well matched with the standard data (JCPDS no. 894319, 19-0629). Meanwhile, the electrode fabricated without an Fe source does not shows any diffraction peaks, which may be due to the absence or low content of crystalline materials. The chemical composition was investigated by SEM-EDS elemental mapping showing the presence of elements such as Fe, Se, O and Ni (Fig. 1h and S3c, SI). Furthermore, HR-TEM images of Ni–Fe_3Se_4 show a *d*-spacing of 0.27 nm, which is well indexed to the (202) orientation and well matched with the XRD data (Fig. S4, SI). Furthermore, Ni–Fe_3Se_4 and Ni–Fe_3O_4 were analysed by Raman spectroscopy (Fig. S6, SI). The Raman spectra of Ni–Fe_3Se_4 show characteristic peaks at 214 cm^{-1} and 240 cm^{-1}, confirming the Fe_3Se_4-type structure of the catalysts.[37] The Raman spectra of Ni–Fe_3O_4 show a peak at 664 cm^{-1}, which is assigned to the A_{1g} mode of vibration.[40]

Catalytic performance for EG and PET oxidation reactions

To evaluate the electrocatalytic performance for electro-oxidation of water, EG and PET hydrolysate, the Ni–Fe_3Se_4 catalyst was directly anchored on nickel foam by facile chemical bath deposition. Self-supported electrodes with direct anchoring of the electrocatalysts on the current collector lead to good adhesion and efficient charge transport, facilitating minimized overpotential loss.[41] Fig. 2a, d and g shows the *iR*-corrected polarization curves for the OER, EGOR and PETOR on working electrodes such as Ni–Fe_3Se_4, Ni–Fe_3O_4 and NiSe. As compared to control electrodes such as NiSe and Ni–Fe_3O_4, self-supported Ni–Fe_3Se_4 exhibited superior catalytic performance, achieving current density of 100 mA cm^{-2} at 1.49 V (*vs.* RHE), 1.37 V (*vs.* RHE) and 1.40 V (*vs.* RHE) for OER, EGOR and PETOR performance, respectively, which is indicating the positive effect of the presence of metal selenide sites[42] (Fig. S7). The OER polarization curve in 1 M KOH electrolyte demonstrates the oxidation peak with an onset potential of 1.30 V (*vs.* RHE),

Open Access Article. Published on 19 November 2025. Downloaded on 12/13/2025 9:16:47 AM.
This article is licensed under a Creative Commons Attribution 3.0 Unported Licence.

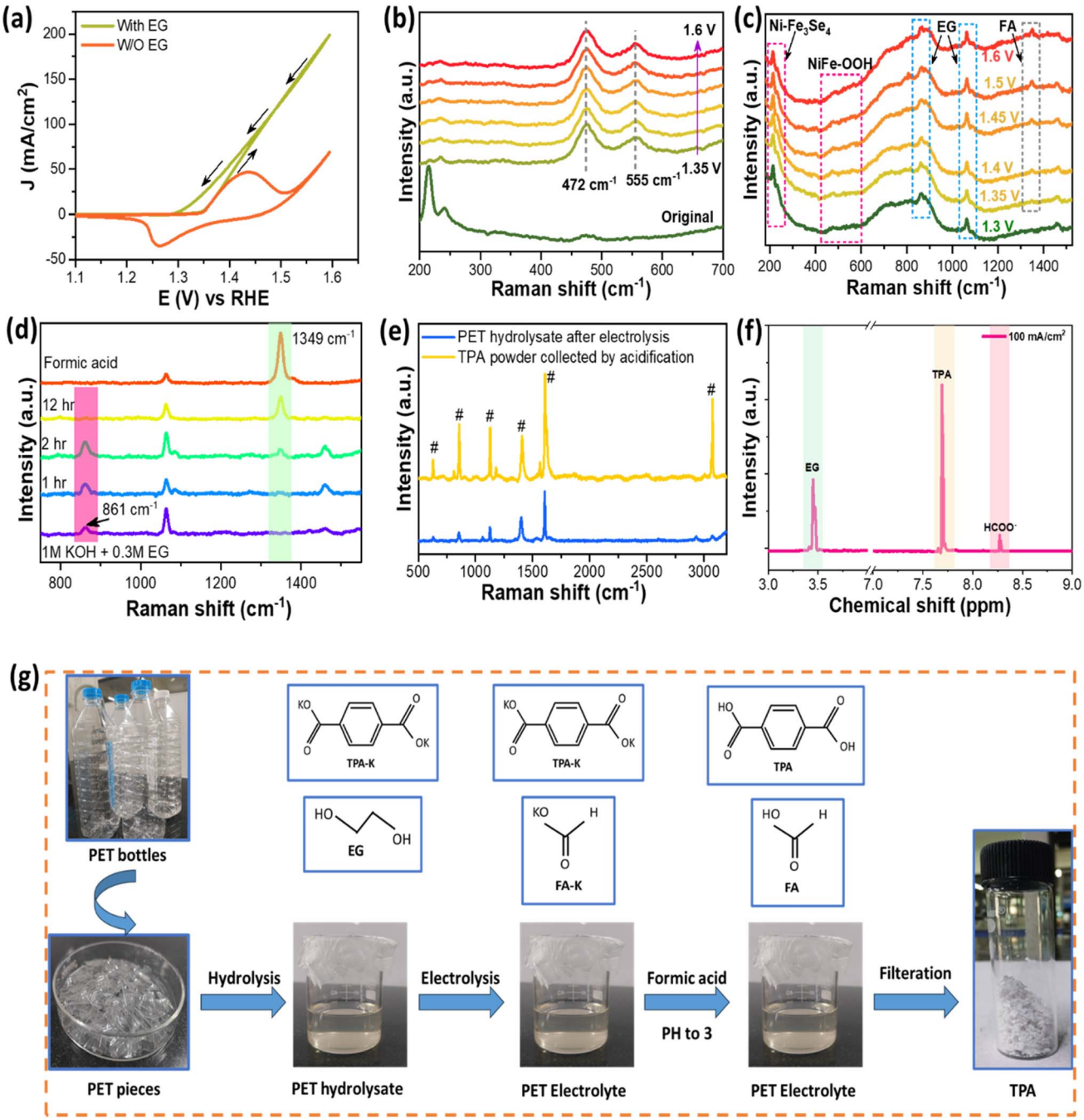

Fig. 3 (a) CV test for Ni–Fe_3Se_4 in 1 M KOH electrolyte with and without (W/O) 0.3 M EG, *in situ* Raman spectroscopy measurements on Ni–Fe_3Se_4 in (b) 1 M KOH electrolyte and (c) 1 M KOH + 0.3 M EG electrolyte, (d) Raman spectra of 1 M KOH + 0.3 EG electrolyte before and after electro-oxidation, (e) Raman spectra of PET hydrolysate after electro-oxidation and PET powder collected by acidification of electrolyte, and (f) ^{1}H NMR spectra of the PET hydrolysate. (g) Schematic diagram of PET plastic upgrading.

suggesting the faradaic charge storage behaviour and redox reaction involved in this process. The OER process on the Ni–Fe_3Se_4 catalyst can be expressed in the following 4 steps:[38]

$$*M + OH_{(aq)}^- \rightarrow *MOH_{ads} + e^- \quad (2)$$

$$*MOH_{ads} + OH_{(aq)\&}^- \rightarrow *MO_{ads} + H_2O + e^- \quad (3)$$

$$*MO_{ads} + OH_{(aq)\&}^- \rightarrow *MOOH_{ads} + H_2O + e^- \quad (4)$$

$$*MOOH_{ads} + OH_{(aq)\&}^- \rightarrow *M + O_2 + H_2O + e^- \quad (5)$$

*M – surface active sites of the Ni–Fe_3Se_4 catalyst.

The redox peak for Ni–Fe_3Se_4 is found to be most intense (except RuO_2), showing the superior electrochemical charge-transport towards the favourable adsorption/desorption of oxygenated species.[43–46] Encouragingly, the onset of the EGOR and PETOR well coincides with the onset of the metal-oxidation

Open Access Article. Published on 19 November 2025. Downloaded on 12/13/2025 9:16:47 AM. This article is licensed under a Creative Commons Attribution 3.0 Unported Licence.

peak of the OER, indicating that the *in situ* formed NiFeOOH sites play the role of catalytically active sites.[7] Owing to the low thermodynamic potential for the EGOR than the OER, Ni–Fe_3Se_4 demonstrates the energy-saving electro-oxidation by lowering the potential by 120 mV for the EGOR and 90 mV for the PETOR. Furthermore, the mechanism of the catalytic performance was further studied using the Tafel plot (Fig. 2b and e). Ni–Fe_3Se_4 possesses the lowest value of the Tafel slope (44.9 mV dec^{-1} for the OER and 15.2 mV dec^{-1} for the EGOR), suggesting the accelerated charge-transport for both the OER and EGOR on Ni–Fe_3Se_4 as compared to NiSe and Ni–Fe_3O_4. Moreover, the lower Tafel value for the EGOR compared to the OER suggests that the EGOR performance is more kinetically favourable than the OER. The charges transport mechanism was further analysed using electrochemical impedance spectroscopy (EIS) (Fig. 2c and f). EIS spectra were recorded in the AC frequency range of 100 kHz to 10 mHz to investigate the charge transfer resistance (R_{ct}). The presence of a semi-circle shows the efficient charge transport at the electrode/electrolyte interface, and lowest value of interfacial charge-transfer resistance for Ni–Fe_3Se_4 for both the OER and EGOR suggests the accelerated charge transport for Ni–Fe_3Se_4, which could lead to higher current densities at small overpotential values. To evaluate the electrochemically active surface area (ECSA), double layer capacitance (C_{dl}) was also estimated (Fig. 2h) using the cyclic voltammetry (CV) curve (Fig. S8, SI). The C_{dl} is found to be higher for Ni–Fe_3Se_4 (2.60 mF cm^{-2}) than NiSe and Ni–Fe_3O_4, which suggests that Ni–Fe_3Se_4 has an abundance of catalytic sites. The catalytic performance of nanostructured electrodes is significantly influenced by ECSA, supporting the superior electro-oxidation performance of the Ni–Fe_3Se_4 catalyst. To further investigate the intrinsic catalytic performance, ECSA normalized polarization curves were calculated (Fig. S9, SI), which show that the Ni–Fe_3Se_4 catalyst exhibited highest normalized current density, indicating its superior intrinsic catalytic performance for the OER, EGOR and PETOR. Additionally, the adsorption of EG on the catalyst surface is a necessity for the EGOR. The direct observation of adsorption of EG on the catalyst surface is difficult as it occurs within the electric double layer.[11] For indirect measurement of EG adsorption, we measure the open-circuit potential (OCP) to study the adsorption of EG on Ni–Fe_3Se_4 catalysts at the macroscopic level. Fig. 2i shows the significant decrease in OCP (0.45 V), suggesting the favourable adsorption of EG on Ni–Fe_3Se_4 catalysts, which leads to accelerated EGOR performance.[11]

Ethylene glycol and PET hydrolysate oxidation reactions

To further explore the active sites and mechanism of the EGOR, cyclic voltammetry curves in 1 M KOH with EG and without EG were recorded (Fig. 3a). The CV curve recorded in the absence of EG shows the obvious oxidation and reduction peaks due to the redox behaviour of Ni and Fe. With EG, CV curves show the onset of the EGOR, coinciding with the onset of the oxidation peak for metals. However, the reduction peak disappears in the presence of EG, which indirectly suggests that the presence of EG suppresses the oxidation of metallic-sites in the Ni–Fe_3Se_4 catalyst. The indirect oxidation mechanism was further confirmed by chronoamperometry tests (Fig. S11, SI). When 1.55 V *vs.* RHE was applied, the oxidation current can be seen indicating the oxidation of metallic-sites. The current with EG is higher due to electro-oxidation of EG. After this, when the reduction potential 1.2 V *vs.* RHE was applied, an obvious reduction current can be seen, suggesting the electrochemical reduction of metallic sites. However, the reduction current suppresses because of the chemically consumed NiFeOOH sites. *In situ* Raman spectroscopy was also performed to further study OER and EGOR performance (Fig. 3b and c). In 1 M KOH, *in situ* Raman spectroscopy shows the original peaks of Ni–Fe_3Se_4 centred at 214 cm^{-1} and 240 cm^{-1} along with the peaks centred at 472 cm^{-1} and 555 cm^{-1} due to NiFeOOH sites generated due to oxidation of Ni–Fe_3Se_4.[47,48] However, the intensity of the peaks for Ni–Fe_3Se_4 has reduced significantly as compared to original data owing to coverage by *in situ* formed NiFeOOH sites on the surface of the Ni–Fe_3Se_4 catalyst. Although, in the presence of EG, peaks of Ni–Fe_3Se_4 and NiFeOOH can be seen, intensity of NiFeOOH is extremely less owing to its chemical reduction, which is well supported by the results of CP and CA tests for the indirect oxidation mechanism. It confirms that *in situ* formed NiFeOOH sites are active sites for EGOR performance.[11] Therefore, the indirect electro-oxidation mechanism proposed by Fleischmann *et al.* can be used to explain the electrochemical oxidation of EG on NiFeOOH.[49–51]

$$M^{2+} \xrightarrow{e^-} M^{3+}$$

$$RCH_2OH_{sol} \rightarrow RCH_2OH_{ads}$$

$$RCH_2OH_{sol} + M^{3+} \xrightarrow{RDS} RCHOH_{ads} + M^{2+}$$

$$RCHOH_{ads} + M^{3+} + H_2O \rightarrow RCOOH_{sol} + M^{2+}$$

The overall electro-oxidation of alcohol follows the aforementioned reaction pathway, wherein the electrocatalyst initially undergoes oxidation to generate the catalytically active NiFeOOH phase. This active species then facilitates the surface reaction, involving the adsorption of alcohol molecules, and the transient formation of a $M(OH)_2$ layer. Under the influence of a high anodic potential, $M(OH)_2$ is rapidly re-oxidized to MOOH, thereby ensuring the continuous regeneration of the active phase and enabling the catalytic cycle to proceed repetitively. Finally, the adsorbed reaction intermediates undergo rapid oxidation, leading to the formation of the corresponding carboxylic acid (RCOOH).

Additionally, the Raman spectrum of the EG electrolyte before electrolysis exhibits three distinct peaks at 861 cm^{-1}, 1064 cm^{-1}, and 1458 cm^{-1} (Fig. 3d), corresponding to the asymmetric stretching vibrations of C–C, C–O, and C–H bonds, respectively.[52,53] For comparison, the Raman spectrum of

Open Access Article. Published on 19 November 2025. Downloaded on 12/13/2025 9:16:47 AM.
This article is licensed under a Creative Commons Attribution 3.0 Unported Licence.

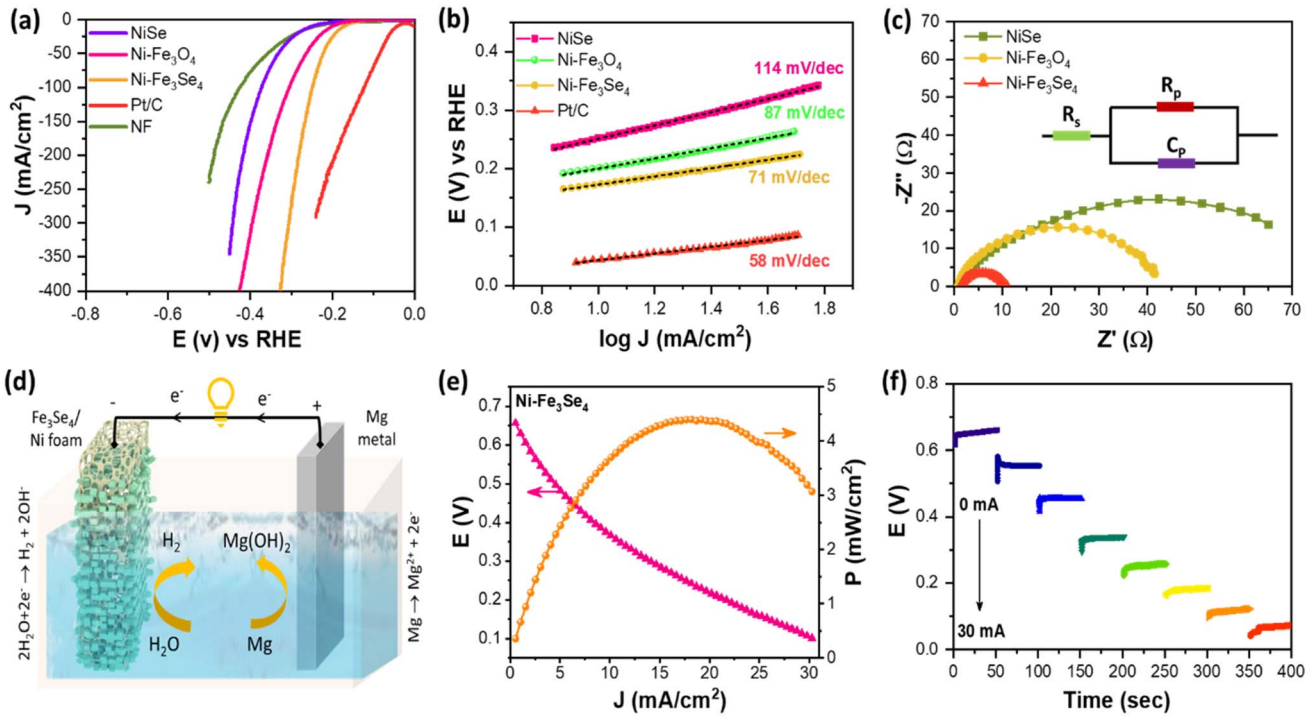

Fig. 4 (a) Polarization curves for HER activity on Ni–Fe_3Se_4, NiSe, Ni–Fe_3O_4, bare NF and commercial Pt/C catalysts, (b) Tafel plots for the HER for all the electrodes, (c) EIS spectra for the HER at 150 mV overpotential, (d) schematic of the Mg–seawater battery based on the Ni–Fe_3Se_4 cathode and its working principle, (e) discharging response along with the corresponding power density of the Mg–seawater battery, and (f) galvanostatic discharging test of the as-fabricated seawater battery at 0 to 30 mA cm^{-2}.

formate (FA) in 1 M KOH solution was also recorded, which shows characteristic peaks at 1061 cm^{-1} and 1344 cm^{-1}, assigned to C–H twisting and bending vibrational modes, respectively.[54,55] The Raman spectra of EG electrolyte at a potential higher that 1.35 V *vs.* RHE display the characteristic vibrational mode at 1344 cm^{-1} associated with FA, alongside the original EG vibrational features, confirming the conversion of EG into FA.

Furthermore, the electro-oxidation of PET hydrolysate and EG electrolyte was accomplished by the chronoamperometry test at 1.6 V *vs.* RHE (without *iR* compensation) (Fig. S12, SI). The observed decrease in current density indicates the progressive depletion of EG in the electrolyte. The Raman spectra of electrolyte after electrolysis for different time intervals were recorded. Notably, intensity of FA vibrational feature increases with time interval, indicating the further conversion of EG into FA. The absence of EG peaks at 12 h suggests minimal residual EG in the electrolyte, corroborating the reduced anodic current observed in the chronoamperometry test. Furthermore, the composition of the product of EG electro-oxidation at different anodic current densities (10–100 mA cm^{-2}) was analysed by ^{1}H NMR spectroscopy and HPLC. As shown in ^{1}H NMR spectra, FA (~8.27 ppm) is the product at all the investigated current densities along with residual EG (~3.45 ppm) (Fig. S13, SI). These results confirm the capabilities of Ni–Fe_3Se_4 catalysts for electro-upcycling of PET into value added products such as terephthalate (TPA) and formate. After electrolysis, PET hydrolysate was further acidified (pH = 3) to facilitate the precipitation of TPA. Raman spectra of the collected TPA (Fig. 3e) confirm its identity, with spectral features consistent with the standard reported data.[56] Fig. 3f shows the ^{1}H NMR spectra of the PET hydrolysate, showing the presence of TPA (~7.69 ppm), residual EG (~3.45 ppm) and FA (~8.27 ppm). HPLC chromatographs confirm the presence of formate after the electrolysis. The quantification of formate and the faradaic efficiency was evaluated. The maximum faradaic efficiency for EG to formate conversion is found to be 89% at a current density of 50 mA cm^{-2} (Fig. S14a and d, SI). Even, the faradaic efficiency of 84% was achieved at a current density of 100 mA cm^{-2}, attributing the capability of Ni–Fe_3Se_4 catalysts for efficient and rapid conversion of EG to value-added products. Fig. 3g and S15 shows the complete process of waste PET bottle upgrading, which consists of mainly three steps: (1) KOH-catalysed waste PET bottle hydrolysis, (2) electro-reforming of PET hydrolysate with electro-oxidation of ethylene glycol (EG), and (3) the separation of TPA and formate.[13,23,57] In conclusion, the electrocatalytic upcycling approach for PET plastics contributes to a closed-loop carbon footprint for plastic waste by facilitating energy-efficient H_2 production in addition to producing value-added compounds as compared to conventional water electrolysis.

Hydrogen evolution reaction and Mg–seawater battery performance with the Ni–Fe_3Se_4 cathode

The kinetics of the HER for the Ni–Fe_3Se_4 catalyst and other control catalysts including NiSe, Ni–Fe_3O_4, bare NF, and

Open Access Article. Published on 19 November 2025. Downloaded on 12/13/2025 9:16:47 AM.
This article is licensed under a Creative Commons Attribution 3.0 Unported Licence.

commercial Pt/C was investigated under alkaline conditions (1 M KOH). Fig. 4a presents the polarization curves for all the catalysts with the *iR*-compensation. The CBD-deposited Ni–Fe_3Se_4 catalyst exhibits enhanced HER activity compared to the NiSe and Ni–Fe_3O_4 control electrodes. Impressively, Ni–Fe_3Se_4 requires an overpotential of 249 mV at a current density of 100 mA cm^{-2}, which is significantly low as compared to control electrodes NiSe (372 mV), Ni–Fe_3O_4 (291 mV), and bare NF (426 mV) and inferior to commercial Pt/C (123 mV). The Tafel slope for the HER on the Ni–Fe_3Se_4 catalyst is 71 mV dec^{-1} (Fig. 4b), the lowest among all the electrodes. Furthermore, the electron transport mechanism and interfacial resistance were investigated by EIS. Fig. 4c shows the Nyquist plots for all the electrodes, showing a minimum charge transfer resistance of 9.7 Ω. It suggests the enhanced conductivity for the Ni–Fe_3Se_4 catalyst, leading to the easy flow of charges. The multi-step chronopotentiometry curves were recorded to analyze the stability of electrodes and charge and mass transport efficiency (Fig. S10b, SI). To illustrate the practicality of the as-prepared catalyst, the Mg–seawater battery was constructed using Ni–Fe_3Se_4 as the cathode, the magnesium alloy (AZ31) as the anode, and simulated seawater (0.5 M NaCl) as the electrolyte (Fig. 4d). Such a battery can provide a long-term power source for underwater devices in the ocean by continuously producing energy by passing electrons from the magnesium electrode to H_2O molecules.[58,59] The polarization curve and the corresponding power density curve of the prepared battery at different current densities are present in Fig. 4e. The open circuit voltage of the prepared battery with the Mg anode is around 0.63 V at 1 mA cm^{-2} current density, which is suddenly decreased with higher

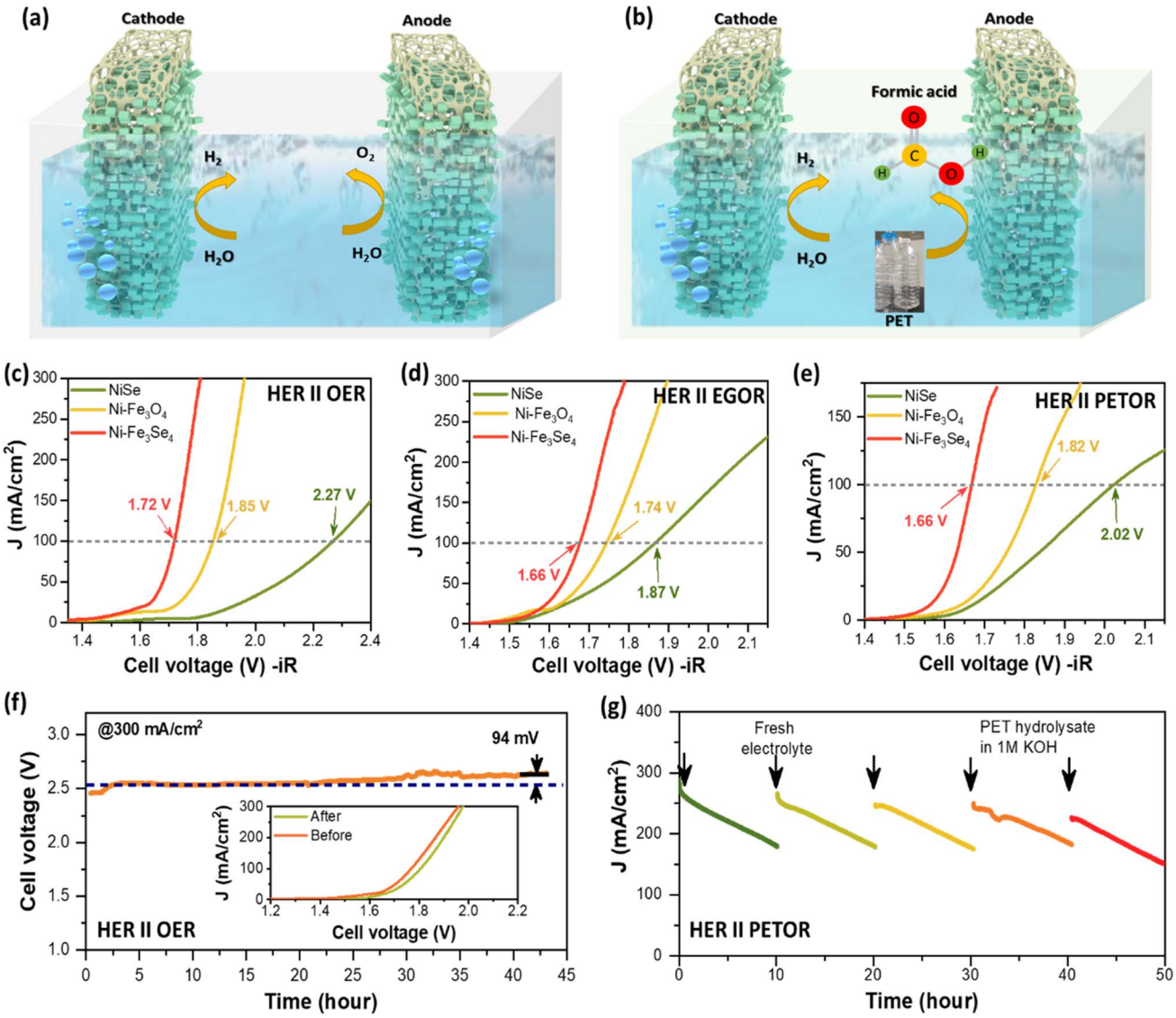

Fig. 5 (a) Schematic representation of the water electrolysis cell, (b) schematic representation of electro-upcycling of PET plastic, polarization curves for bi-functional electrolysis on Ni–Fe_3Se_4, Ni–Fe_3O_4 and NiSe (with *iR* compensation): (c) 1 M KOH, (d) 1 M KOH + 0.3 M EG, and (e) 1 M KOH + PET, (f) long-term stability test for water electrolysis on Ni–Fe_3Se_4 at 300 mA cm^{-2} (potential is without *iR* compensation), and (g) long-term stability test for PET electro-upcycling over 5 cycles using Ni–Fe_3Se_4 electrodes.

Open Access Article. Published on 19 November 2025. Downloaded on 12/13/2025 9:16:47 AM.
This article is licensed under a Creative Commons Attribution 3.0 Unported Licence.

current density. The high open circuit value may be due to the presence of dissolved oxygen in the electrolyte, which rapidly decreased after the trace of oxygen was consumed.[59] Furthermore, the Mg–seawater battery with Ni–Fe_3Se_4 catalysts as the cathode shows a maximum power density of 4.4 mW cm^{-2} at 18 mA cm^{-2} current density, which suggests a highly promising result. The discharge curve of the prepared Mg–seawater battery with different current densities is displayed in Fig. 4f, which demonstrates that such devices work stably at different current densities, indicating its exceptional stability.

Industrial scale overall water electrolysis and PET upgrading

Fig. 5a schematically depicts a two-electrode alkaline electrolyser with Ni–Fe_3Se_4 based electrodes as the anode and cathode, which was analyzed at both laboratory (1 M KOH) and industrial scales (3 M, 5 M KOH). When the cell voltage was applied, there was vigorous gas bubbling from both electrodes, suggesting that H_2 and O_2 were being produced simultaneously. Polarization curves for Ni–Fe_3Se_4 electrodes in alkaline electrolyte indicate the obvious electrolysis of water, producing the geometric current densities of 10 and 100 mA cm^{-2} at cell voltages of 1.52 V and 1.72 V (Fig. 5c). The cell voltage was further reduced to 1.70 V and 1.68 V to generate 100 mA cm^{-2} in high-concentration (3 M, and 5 M) alkaline electrolytes (Fig. S16a, SI). For further advancement of the electrolysis, the catalytic performance is measured at elevated temperature up to 60 °C (Fig. S16b, SI). The cell voltage at 100 mA cm^{-2} is found to reduce from 1.68 V at 25 °C to 1.57 V at 60 °C. Electrochemical impedance spectroscopy (EIS) was also carried out at 1.5 V to understand the charge transfer during the electrocatalytic reaction (Fig. S17, SI). The stable catalytic performance is extremely important to develop the robust electrodes for sustainable and cost-efficient H_2-synthesis. The multi-step chrono-potentiometry curves were recorded at current densities ranging from 10 to 400 mA cm^{-2}, showing the steep switching of cell voltage upon change in current as well as stable cell voltage at all the current values (Fig. S18). Furthermore, the dimensional stability and robustness of electrochemical performance for water electrolysis were measured at an industrial scale current density of 300 mA cm^{-2} for the time interval of 42 hours (Fig. 5f). The polarization curves for water electrolysis (inset, Fig. 5f) shows slight shifting of 20 mV on the higher potential side after 42 h of the stability test, suggesting the capability of the Ni–Fe_3Se_4 catalyst for sustainable hydrogen production and also bridging the gap between the fundamental research and the industrial scale water electrolysis for green H_2 and O_2 production.

Considering the high abundance of catalytically active sites and the great potential of Ni–Fe_3Se_4 for ethylene glycol oxidation under diverse conditions, an ethylene glycol and PET hydrolysate electrolyzer was developed. The present system enables the transformation of waste into value-added products, including hydrogen (H_2) production, anodic oxidation of ethylene glycol into formate, and the generation of terephthalate (TPA) (Fig. 5b). The PET and EG electrolyser requires a cell voltage of 1.66 V to generate 100 mA cm^{-2} current, which is 60 mV smaller than the cell voltage required for water electrolysis, suggesting the saving of electric energy due to readily oxidized nature of the EG molecule (Fig. 5c and e). For production of 1 Nm^3 of H_2, the electricity consumption is 4.2 kWh Nm^{-3} and 4.0 kWh Nm^{-3} for conventional water electrolysis and PET hydrolysate electrolysis. Furthermore, chronoamperometry (CA) tests were executed over 5-consecutive cycles of PET hydrolysate electrolysis at initial current densities exceeding 250 mA cm^{-2}, demonstrating the excellent stability of the system. The decrease in current density in the CA-test can be attributed to the depletion of ethylene glycol (EG) concentration in electrolyte during electrolysis (Fig. 5g). However, the high current response is restored upon replacing the electrolysed electrolyte with fresh PET hydrolysate, highlighting the robust nature of the Ni–Fe_3Se_4 catalyst. This demonstrates its excellent stability and catalytic efficiency, ensuring sustained performance over multiple cycles for transforming waste into value-added products. Additionally, the Ni–Fe_3Se_4 electrode was analysed by XPS after the stability test (Fig. S19). There is no significant change in the electronic structure after long term stability, suggesting the robustness of the electrode. The superior performance of the Ni–Fe_3Se_4 catalyst for industrial scale water electrolysis and PET electro-upcycling can be attributed to several factors such as (i) high electrochemically active surface area due to abundance of active sites, as confirmed by SEM and C_{dl} values; (ii) reduced charge transfer resistance; (iii) *in situ* formed NiFeOOH centres for efficient anodic oxidation reactions.

Conclusions

In summary, we demonstrated the electro-upcycling of PET plastic coupled with H2-production using a Ni–Fe_3Se_4 catalyst. The nanostructured morphology of Ni–Fe_3Se_4 provides a high specific surface area, abundant active sites, and rapid charge transfer, resulting in exceptional performance for water electrolysis, PET upgrading and ethylene glycol electrolysis. The Ni–Fe_3Se_4 catalysts demonstrated superior catalytic activity, achieving low overpotentials of 174 mV for the hydrogen evolution reaction (HER) and 164 mV for the oxygen evolution reaction (OER) at a current density of 10 mA cm^{-2}. These values surpass those of previously reported catalysts. Additionally, Ni–Fe_3Se_4 exhibited excellent corrosion resistance and dimensional stability, enabling efficient water electrolysis under industrial alkaline conditions (5 M KOH) and at industrial-scale current densities. Stability testing confirmed electrode durability, maintaining performance at 300 mA cm^{-2} for over 42 hours. Furthermore, we developed and evaluated an Mg/seawater battery that combined Mg oxidation with the HER, which can generate the required power for the electrolysis, enabling development of the self-powered electrolyser. The Mg/seawater battery, employing Ni–Fe_3Se_4 as the cathode material, delivered a peak power density of 4.4 mW cm^{-2} at a current density of 18 mA cm^{-2}. Additionally, electrolysis of PET hydrolysate at 1.667 V enabled PET plastic electro-upcycling at a current density of 100 mA cm^{-2}, yielding value-added products such as formate with a faradaic efficiency of 89% and terephthalate due

 This journal is © The Royal Society of Chemistry 2025

Open Access Article. Published on 19 November 2025. Downloaded on 12/13/2025 9:16:47 AM. This article is licensed under a Creative Commons Attribution 3.0 Unported Licence.

to abundance of *in situ* formed NiFeOOH sites. This work highlights a simple and effective approach to developing cost-effective electrodes, demonstrating their potential for industrial-scale water splitting for H_2 production and upcycling the PET plastic waste.

Conflicts of interest

The authors declare that they have no known competing financial interests or personal relationships that could have appeared to influence the work reported in this paper.

Data availability

Data will be made available on request.

Supplementary information (SI) is available. See DOI: https://doi.org/10.1039/d5ta06515a.

Acknowledgements

The authors are thankful to the Gujarat State Biotechnology Mission (GSBTM/JD/(R&D)/662/2022-23/00292122) for the financial support. We are also thankful to Department of Science & Technology (DST-PURSE) (SR/PURSE/2023/162) for the instrumental support (*in situ* EC-Raman spectroscopy). The authors are thankful to CHARUSAT for providing research facilities.

References

1 M. Jiang, X. Wang, W. Xi, P. Yang, H. Zhou, J. Duan, M. Ratova and D. Wu, Chemical catalytic upgrading of polyethylene terephthalate plastic waste into value-added materials, fuels and chemicals, *Sci. Total Environ.*, 2024, **912**, 169342, DOI: 10.1016/j.scitotenv.2023.169342.

2 L. D. Ellis, N. A. Rorrer, K. P. Sullivan, M. Otto, J. E. McGeehan, Y. Román-Leshkov, N. Wierckx and G. T. Beckham, Chemical and biological catalysis for plastics recycling and upcycling, *Nat. Catal.*, 2021, **4**, 539–556, DOI: 10.1038/s41929-021-00648-4.

3 Y. Jiang, H. Zhang, L. Hong, J. Shao, B. Zhang, J. Yu and S. Chu, An Integrated Plasma–Photocatalytic System for Upcycling of Polyolefin Plastics, *ChemSusChem*, 2023, **16**, e202300106, DOI: 10.1002/cssc.202300106.

4 M. G. Kibria, N. I. Masuk, R. Safayet, H. Q. Nguyen and M. Mourshed, Plastic Waste: Challenges and Opportunities to Mitigate Pollution and Effective Management, *Int. J. Environ. Res.*, 2023, **17**, 20, DOI: 10.1007/s41742-023-00507-z.

5 P. G. C. N. T. Pilapitiya and A. S. Ratnayake, The world of plastic waste: a review, *Cleaner Mater.*, 2024, **11**, 100220, DOI: 10.1016/j.clema.2024.100220.

6 Y. Li, L. Tao, Q. Wang, F. Wang, G. Li and M. Song, Potential Health Impact of Microplastics: A Review of Environmental Distribution, Human Exposure, and Toxic Effects, *Environ. Health*, 2023, **1**, 249–257, DOI: 10.1021/envhealth.3c00052.

7 K. Liu, Y. Wang, F. Liu, C. Liu, R. Shi and Y. Chen, Selective electrocatalytic reforming of PET-derived ethylene glycol to formate with a Faraday efficiency of 93.2% at industrial-level current densities, *Chem. Eng. J.*, 2023, **473**, 145292, DOI: 10.1016/j.cej.2023.145292.

8 J. J. R. Arias and W. Thielemans, Instantaneous hydrolysis of PET bottles: an efficient pathway for the chemical recycling of condensation polymers, *Green Chem.*, 2021, **23**, 9945–9956, DOI: 10.1039/D1GC02896K.

9 H. Kang, D. He, X. Yan, B. Dao, N. B. Williams, G. I. Elliott, D. Streater, J. Nyakuchena, J. Huang, X. Pan, X. Xiao and J. Gu, Cu Promoted the Dynamic Evolution of Ni-Based Catalysts for Polyethylene Terephthalate Plastic Upcycling, *ACS Catal.*, 2024, **14**, 5314–5325, DOI: 10.1021/acscatal.3c05509.

10 Z. Chen, R. Zheng, T. Bao, T. Ma, W. Wei, Y. Shen and B.-J. Ni, Dual-Doped Nickel Sulfide for Electro-Upgrading Polyethylene Terephthalate into Valuable Chemicals and Hydrogen Fuel, *Nano-Micro Lett.*, 2023, **15**, 210, DOI: 10.1007/s40820-023-01181-8.

11 W. Li, D. Xiao, X. Gong, X. Xu, F. Ma, Z. Wang, P. Wang, Y. Liu, Y. Dai, Z. Zheng, Y. Fan and B. Huang, Electrocatalytic upgrading of polyethylene terephthalate plastic to formic acid at an industrial-scale current density via Ni-MOF @ MnCo-OH catalyst, *Chem. Eng. J.*, 2024, **480**, 148087, DOI: 10.1016/j.cej.2023.148087.

12 F. Liu, X. Gao, R. Shi, E. C. M. Tse and Y. Chen, A general electrochemical strategy for upcycling polyester plastics into added-value chemicals by a CuCo2O4 catalyst, *Green Chem.*, 2022, **24**, 6571–6577, DOI: 10.1039/D2GC02049A.

13 J. Wang, X. Li, M. Wang, T. Zhang, X. Chai, J. Lu, T. Wang, Y. Zhao and D. Ma, Electrocatalytic Valorization of Poly(ethylene terephthalate) Plastic and CO2 for Simultaneous Production of Formic Acid, *ACS Catal.*, 2022, **12**, 6722–6728, DOI: 10.1021/acscatal.2c01128.

14 F. Ma, Z. Li, R. Hu, Z. Wang, J. Wang, J. Li, Y. Nie, Z. Zheng and X. Jiang, Electrocatalytic Waste-Treating-Waste Strategy for Concurrently Upgrading of Polyethylene Terephthalate Plastic and CO2 into Value-Added Formic Acid, *ACS Catal.*, 2023, **13**, 14163–14172, DOI: 10.1021/acscatal.3c03428.

15 D. Si, B. Xiong, L. Chen and J. Shi, Highly selective and efficient electrocatalytic synthesis of glycolic acid in coupling with hydrogen evolution, *Chem Catal.*, 2021, **1**, 941–955, DOI: 10.1016/j.checat.2021.08.001.

16 Z. Li, Z. Yang, S. Wang, H. Luo, Z. Xue, Z. Liu and T. Mu, Medium entropy metal oxide induced *OH species targeted transfer strategy for efficient polyethylene terephthalate plastic recycling, *Chem. Eng. J.*, 2024, **479**, 147611, DOI: 10.1016/j.cej.2023.147611.

17 Y. Zhong, Z. Wu, X. Liu and L. Li, Prismatic Al-MOF composite rGO immobilized PdBiMn alloy catalyst for facilitating ethylene glycol electrooxidation, *Colloids Surf., A*, 2022, **652**, 129672, DOI: 10.1016/j.colsurfa.2022.129672.

18 S. F. Zai, Y. H. Wu, Y. T. Zhou, Z. T. H. Li and C. B. Guo, Hierarchical NiOx nanotube arrays/CoP nanosheets heterostructure enables robust alkaline hydrogen evolution reaction, *J. Colloid Interface Sci.*, 2023, **643**, 350–359, DOI: 10.1016/j.jcis.2023.04.043.

Open Access Article. Published on 19 November 2025. Downloaded on 12/13/2025 9:16:47 AM.
This article is licensed under a Creative Commons Attribution 3.0 Unported Licence.

19 Y. Katayama, T. Okanishi, H. Muroyama, T. Matsui and K. Eguchi, Enhanced Supply of Hydroxyl Species in CeO2-Modified Platinum Catalyst Studied by in Situ ATR-FTIR Spectroscopy, *ACS Catal.*, 2016, **6**, 2026–2034, DOI: 10.1021/acscatal.6b00108.

20 H. Wang, B. Jiang, T.-T. Zhao, K. Jiang, Y.-Y. Yang, J. Zhang, Z. Xie and W.-B. Cai, Electrocatalysis of Ethylene Glycol Oxidation on Bare and Bi-Modified Pd Concave Nanocubes in Alkaline Solution: An Interfacial Infrared Spectroscopic Investigation, *ACS Catal.*, 2017, **7**, 2033–2041, DOI: 10.1021/acscatal.6b03108.

21 L. Xin, Z. Zhang, J. Qi, D. Chadderdon and W. Li, Electrocatalytic oxidation of ethylene glycol (EG) on supported Pt and Au catalysts in alkaline media: reaction pathway investigation in three-electrode cell and fuel cell reactors, *Appl. Catal., B*, 2012, **125**, 85–94, DOI: 10.1016/j.apcatb.2012.05.024.

22 P. Song, H. Xu, J. Wang, Y. Shiraishi and Y. Du, Construct 3D networked Au-Cu nanowires for enhanced plasmon-driven catalytic ethylene glycol oxidation through visible light irradiation, *J. of Power Sources*, 2018, **399**, 59, DOI: 10.1016/j.jpowsour.2018.07.083.

23 H. Zhou, Y. Ren, Z. Li, M. Xu, Y. Wang, R. Ge, X. Kong, L. Zheng and H. Duan, Electrocatalytic upcycling of polyethylene terephthalate to commodity chemicals and H2 fuel, *Nat. Commun.*, 2021, **12**, 4679, DOI: 10.1038/s41467-021-25048-x.

24 X. Zou, Y. Liu, G.-D. Li, Y. Wu, D.-P. Liu, W. Li, H.-W. Li, D. Wang, Y. Zhang and X. Zou, Ultrafast Formation of Amorphous Bimetallic Hydroxide Films on 3D Conductive Sulfide Nanoarrays for Large-Current-Density Oxygen Evolution Electrocatalysis, *Adv. Mater.*, 2017, **29**, 1700404, DOI: 10.1002/adma.201700404.

25 M. Du, Y. Zhang, S. Kang, C. Xu, Y. Ma, L. Cai, Y. Zhu, Y. Chai and B. Qiu, Electrochemical Production of Glycolate Fuelled By Polyethylene Terephthalate Plastics with Improved Techno-Economics, *Small*, 2023, **19**, 2303693, DOI: 10.1002/smll.202303693.

26 P. J. Sharma, K. H. Modi, P. Sahatiya, C. K. Sumesh and P. M. Pataniya, Electroless deposited NiP-fabric electrodes for efficient water and urea electrolysis for hydrogen production at industrial scale, *Appl. Surf. Sci.*, 2024, **644**, 158766, DOI: 10.1016/j.apsusc.2023.158766.

27 X. Du, M. A. Oturan, M. Zhou, N. Belkessa, P. Su, J. Cai, C. Trellu and E. Mousset, Nanostructured electrodes for electrocatalytic advanced oxidation processes: from materials preparation to mechanisms understanding and wastewater treatment applications, *Appl. Catal., B*, 2021, **296**, 120332, DOI: 10.1016/J.APCATB.2021.120332.

28 F. E. Titchou, H. Zazou, H. Afanga, J. El Gaayda, R. A. Akbour, P. V. Nidheesh and M. Hamdani, An overview on the elimination of organic contaminants from aqueous systems using electrochemical advanced oxidation processes, *J. Water Process Eng.*, 2021, **41**, 102040, DOI: 10.1016/J.JWPE.2021.102040.

29 Y. Liu, X. Liang, L. Gu, Y. Zhang, G.-D. Li, X. Zou and J.-S. Chen, Corrosion engineering towards efficient oxygen evolution electrodes with stable catalytic activity for over 6000 hours, *Nat. Commun.*, 2018, **9**, 2609, DOI: 10.1038/s41467-018-05019-5.

30 K. Zhang, Y. Li, S. Deng, S. Shen, Y. Zhang, G. Pan, Q. Xiong, Q. Liu, X. Xia and X. Wang, Molybdenum selenide electrocatalysts for electrochemical hydrogen evolution reaction, *ChemElectroChem*, 2019, **6**, 3530–3548.

31 C. Tang, N. Cheng, Z. Pu, W. Xing and X. Sun, NiSe nanowire film supported on nickel foam: an efficient and stable 3D bifunctional electrode for full water splitting, *Angew. Chem.*, 2015, **127**, 9483–9487.

32 B. Jing, S. You, Y. Ma, Z. Xing, H. Chen, Y. Dai, C. Zhang, N. Ren and J. Zou, Fe3Se4/FeSe heterojunctions in cornstalk-derived N-doped carbon framework enhance charge transfer and cathodic oxygen reduction reaction to boost bio-electricity generation, *Appl. Catal., B*, 2019, **244**, 465–474.

33 H. Liu, F. Yang, F. Chen, S. Che, N. Chen, S. Sun, N. Ta, Y. Sun, N. Wu and Y. Sun, Interface and electronic structure regulation of Mo-doped NiSe2-CoSe2 heterostructure aerogel for efficient overall water splitting, *J. Colloid Interface Sci.*, 2023, **640**, 1040–1051.

34 B. Wang, K. Srinivas, X. Wang, Z. Su, B. Yu, Y. Liu, F. Ma, D. Yang and Y. Chen, Self-assembled CoSe 2–FeSe 2 heteronanoparticles along the carbon nanotube network for boosted oxygen evolution reaction, *Nanoscale*, 2021, **13**, 9651–9658.

35 B. Mohanty, B. K. Jena, M. Kandasamy, N. Dalai, R. K. Sahu, R. M. Kadam, B. Chakraborty and B. Jena, The role of Se vacancies and Fe doping of nickel selenide in the water oxidation reaction, *Sustainable Energy Fuels*, 2020, **4**, 3058–3065.

36 Z. Huang, P. Li, M. Feng, W. Zhu, A. R. Woldu, Q.-X. Tong and L. Hu, Unlocking Fe(III) Ions Improving Oxygen Evolution Reaction Activity and Dynamic Stability of Anodized Nickel Foam, *Inorg. Chem.*, 2024, **63**, 15493–15502, DOI: 10.1021/acs.inorgchem.4c02646.

37 N. Hussain, M. Kiran, Z. Gao, L. Tang, J. Li, P. Gao, Z. Chen, F. Li and T. Liu, Hierarchically Porous Donut-Like Fe3Ni2Se4 Bimetallic Selenide: An Ultra-High-Rate Anode for Potassium Ions Storage, *Adv. Funct. Mater.*, 2024, **34**, 2310805, DOI: 10.1002/adfm.202310805.

38 R. Manikandan, C. J. Raj, G. Nagaraju, R. Velayutham, S. E. Moulton, J. Puigdollers and B. C. Kim, Selenium enriched hybrid metal chalcogenides with enhanced redox kinetics for high-energy density supercapacitors, *Chem. Eng. J.*, 2021, **414**, 128924, DOI: 10.1016/j.cej.2021.128924.

39 N.-N. Song, H.-T. Yang, H.-L. Liu, X. Ren, H.-F. Ding, X.-Q. Zhang and Z.-H. Cheng, Exceeding natural resonance frequency limit of monodisperse Fe3O4 nanoparticles via superparamagnetic relaxation, *Sci. Rep.*, 2013, **3**, 3161, DOI: 10.1038/srep03161.

40 R. Jaiswal and K. V. S. Ranganath, Carbon Nanoparticles on Magnetite: A New Heterogeneous Catalyst for the Oxidation of 5-Hydroxymethylfurfural (5-HMF) to 2,5-Diformoylfuran (DFF), *J. Inorg. Organomet. Polym. Mater.*, 2021, **31**, 4504–4511, DOI: 10.1007/s10904-021-02062-6.

 This journal is © The Royal Society of Chemistry 2025

Open Access Article. Published on 19 November 2025. Downloaded on 12/13/2025 9:16:47 AM.
This article is licensed under a Creative Commons Attribution 3.0 Unported Licence.

41 H. Yang, M. Driess and P. W. Menezes, Self-Supported Electrocatalysts for Practical Water Electrolysis, *Adv. Energy Mater.*, 2021, **11**, 2102074, DOI: 10.1002/aenm.202102074.

42 S. Duan, S. Chen, T. Wang, S. Li, J. Liu, J. Liang, H. Xie, J. Han, S. Jiao, R. Cao, H.-L. Wang and Q. Li, Elemental selenium enables enhanced water oxidation electrocatalysis of NiFe layered double hydroxides, *Nanoscale*, 2019, **11**, 17376–17383, DOI: 10.1039/C9NR06169J.

43 Y. Niu, W. Li, X. Wu, B. Feng, Y. Yu, W. Hu and C. M. Li, Amorphous nickel sulfide nanosheets with embedded vanadium oxide nanocrystals on nickel foam for efficient electrochemical water oxidation, *J. Mater. Chem. A*, 2019, **7**, 10534–10542, DOI: 10.1039/C8TA12483C.

44 Z. Liu, N. Li, H. Zhao, Y. Zhang, Y. Huang, Z. Yin and Y. Du, Regulating the active species of Ni(OH)2 using CeO2: 3D CeO2/Ni(OH)2/carbon foam as an efficient electrode for the oxygen evolution reaction, *Chem. Sci.*, 2017, **8**, 3211–3217, DOI: 10.1039/C6SC05408K.

45 L. Trotochaud, S. L. Young, J. K. Ranney and S. W. Boettcher, Nickel-Iron oxyhydroxide oxygen-evolution electrocatalysts: the role of intentional and incidental iron incorporation, *J. Am. Chem. Soc.*, 2014, **136**, 6744, DOI: 10.1021/ja502379c.

46 J.-G. Li, H. Sun, L. Lv, Z. Li, X. Ao, C. Xu, Y. Li and C. Wang, Metal–Organic Framework-Derived Hierarchical (Co,Ni) Se2@NiFe LDH Hollow Nanocages for Enhanced Oxygen Evolution, *ACS Appl. Mater. Interfaces*, 2019, **11**, 8106–8114, DOI: 10.1021/acsami.8b22133.

47 B. M. Kathale, H. Xiao, S. Yang, H. Yin, T. Yu, X. Zhou, L. Qian, J. Xiao, P. Lei and X. Li, Fluoride mediated conversion of FeOOH into NiFeOOH for outstanding oxygen evolution reaction, *Electrochim. Acta*, 2022, **406**, 139831, DOI: 10.1016/j.electacta.2022.139831.

48 X. Luo, H. Zhao, X. Tan, S. Lin, K. Yu, X. Mu, Z. Tao, P. Ji and S. Mu, Fe-S dually modulated adsorbate evolution and lattice oxygen compatible mechanism for water oxidation, *Nat. Commun.*, 2024, **15**, 8293, DOI: 10.1038/s41467-024-52682-y.

49 M. T. Bender, Y. C. Lam, S. Hammes-Schiffer and K.-S. Choi, Unraveling two pathways for electrochemical alcohol and aldehyde oxidation on NiOOH, *J. Am. Chem. Soc.*, 2020, **142**, 21538–21547.

50 M. T. Bender, R. E. Warburton, S. Hammes-Schiffer and K.-S. Choi, Understanding hydrogen atom and hydride transfer processes during electrochemical alcohol and aldehyde oxidation, *ACS Catal.*, 2021, **11**, 15110–15124.

51 F. Ma, S. Wang, L. Han, Y. Guo, Z. Wang, P. Wang, Y. Liu, H. Cheng, Y. Dai and Z. Zheng, Targeted regulation of the electronic states of nickel toward the efficient electrosynthesis of benzonitrile and hydrogen production, *ACS Appl. Mater. Interfaces*, 2021, **13**, 56140–56150.

52 S. Cersoy, V. Rouchon, O. Belhadj, J. Cuisin and M. Herbin, Noninvasive Fluid Identification: Potential of Micro-Raman Spectroscopy, *Collect. Forum*, 2021, **34**, 53–72, DOI: 10.14351/0831-4985-34.1.53.

53 S. O. Liubimovskii, V. S. Novikov, L. Y. Ustynyuk, P. V. Ivchenko, K. A. Prokhorov, V. V. Kuzmin, E. A. Sagitova, M. M. Godyaeva, S. V. Gudkov and M. E. Darvin, Spectrochimica Acta Part A: Molecular and Biomolecular Spectroscopy Raman structural study of ethylene glycol and 1, 3-propylene glycol aqueous solutions, *Spectrochim. Acta, Part A*, 2023, **285**, 121927, DOI: 10.1016/j.saa.2022.121927.

54 G. Wu, X. Dong, J. Mao, G. Li, C. Zhu and S. Li, Anodic glycerol oxidation to formate facilitating cathodic hydrogen evolution with earth-abundant metal oxide catalysts, *Chem. Eng. J.*, 2023, **468**, 143640, DOI: 10.1016/j.cej.2023.143640.

55 Z. He, J. Hwang, Z. Gong, M. Zhou, N. Zhang, X. Kang, J. W. Han and Y. Chen, Promoting biomass electrooxidation via modulating proton and oxygen anion deintercalation in hydroxide, *Nat. Commun.*, 2022, **13**, 3777, DOI: 10.1038/s41467-022-31484-0.

56 M. W. Lee, M. S. Kim and K. Kim, Infrared and Raman spectroscopic study of terephthalic acid adsorbed on silver surfaces, *J. Mol. Struct.*, 1997, **415**, 93–100, DOI: 10.1016/S0022-2860(97)00081-1.

57 Y. Li, L. Q. Lee, Z. G. Yu, H. Zhao, Y.-W. Zhang, P. Gao and H. Li, Coupling of PET waste electroreforming with green hydrogen generation using bifunctional catalyst, *Sustainable Energy Fuels*, 2022, **6**, 4916–4924.

58 P. K. Shen, A. C. C. Tseung and C. Kuo, Development of an aluminium/sea water battery for sub-sea applications, *J. Power Sources*, 1994, **47**, 119–127.

59 Q. Liu, Z. Yan, E. Wang, S. Wang and G. Sun, A high-specific-energy magnesium/water battery for full-depth ocean application, *Int. J. Hydrogen Energy*, 2017, **42**, 23045–23053.